

# Anisotropic complex electrical conductivity of black shale and mudstone from the Moffat Shale Group (Ireland)

L. Römhild<sup>1</sup>, M. Sonntag<sup>1</sup>, D. Kiyan<sup>2,3</sup>, R. Rogers<sup>4</sup>, V. Rath<sup>2,5</sup> and J.H. Börner<sup>1\*</sup>

<sup>1</sup>Institute of Geophysics and Geoinformatics, Technical University Bergakademie Freiberg, Freiberg, Germany, <sup>2</sup>Geophysics Section, School of Cosmic Physics, Dublin Institute for Advanced Studies, Dublin, Ireland, <sup>3</sup>Irish Centre for Research in Applied Geosciences, iCRAG, Dublin, Ireland, <sup>4</sup>Geological Survey Ireland, Dublin, Ireland, and <sup>5</sup>ISTerre, Université Savoie Montblanc, Le Bourget du Lac, France

Received April 2019, revision accepted October 2019

## ABSTRACT

The geological setting in the north of Ireland, especially concerning the origin of the Moffat Shale Group, has long been under discussion. Within the Tellus Programme of the Geological Survey Ireland, airborne electromagnetic measurements revealed high-conductivity anomalies that have been interpreted as the response of a black shale. In order to petrophysically characterize the Moffat Shale, a laboratory study using material from two shallow boreholes was carried out. The study focuses on spectral induced polarization measurements on 23 oriented samples in the frequency range from  $10^{-4}$  to  $10^5$  Hz.

The sample material can be categorized into two groups. A mudstone-like rock type shows weakly frequency-dependent, porosity-driven conductivities with a strong anisotropy. On the other hand, black shale samples are characterized by moderately anisotropic but strong polarization effects especially at low frequencies and a strong conductivity increase towards higher frequencies. The polarization in the black shale is controlled by the texture and volume fraction of the polarizable components. The spectral induced polarization data are processed by means of a Debye decomposition approach. The anisotropy of the complex electrical conductivity is determined by utilizing the foliation dip angle and assuming tilted transverse isotropic conditions. The relevance of the laboratory findings for airborne electromagnetic surveys is addressed with a synthetic one-dimensional modelling study.

**Key words:** Airborne EM, Complex Conductivity, Chargeability, Induced Polarization, Shallow Subsurface.

## INTRODUCTION

Airborne electromagnetic (AEM) surveys in frequency or time domain are a common tool to efficiently map the geological structure of the subsurface and potential natural resources of large areas. They provide extensive information about the upper 10 to 100 m with a high spatial resolution (e.g. Fountain 1998; Siemon, Auken and Christiansen 2009a; Arab-Amiri *et al.* 2010; Götze *et al.* 2014; Li *et al.* 2017). More and more sophisticated inversion schemes and tools are available, which are able to deal also with large three-dimensional

AEM datasets (e.g. Siemon Auken and Christiansen 2009b; Pfaffhuber, Hendricks and Kvistedal 2012; Auken *et al.* 2015; Scheunert *et al.* 2016; Anshütz *et al.* 2017; Kiyan, Rath and Delhay 2017; McMillan, Haber and Marchant 2018). The impact of specific petrophysical settings, such as rocks with strong electrical polarization properties (i.e. induced polarization) is subject to recent and current research (e.g. Kratzer and Macnae 2012; Lin *et al.* 2019). The effect of anisotropy has been studied by means of numerical simulations (e.g. Avdeev *et al.* 1998; Liu and Yin 2014).

In the course of the Tellus Programme, which is carried out by the Geological Survey Ireland, AEM frequency

\*E-mail: jana.boerner@geophysik.tu-freiberg.de

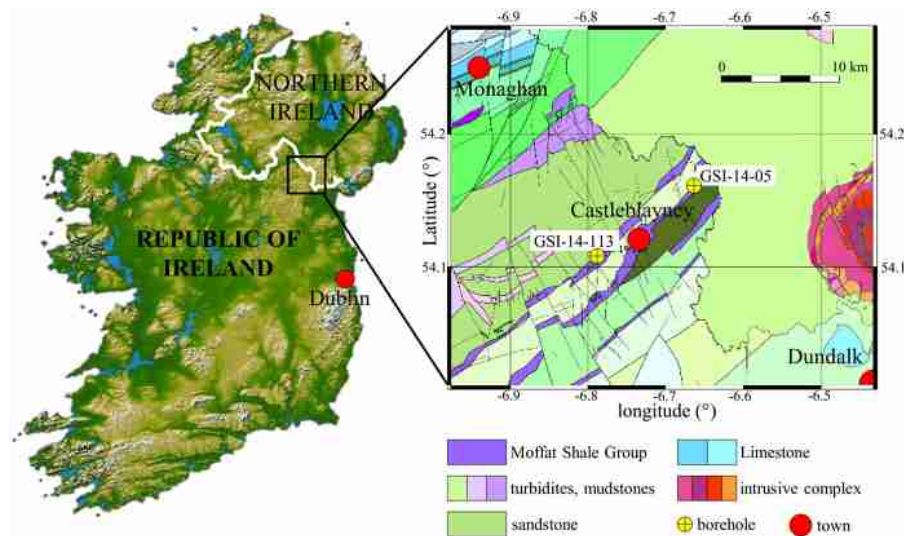


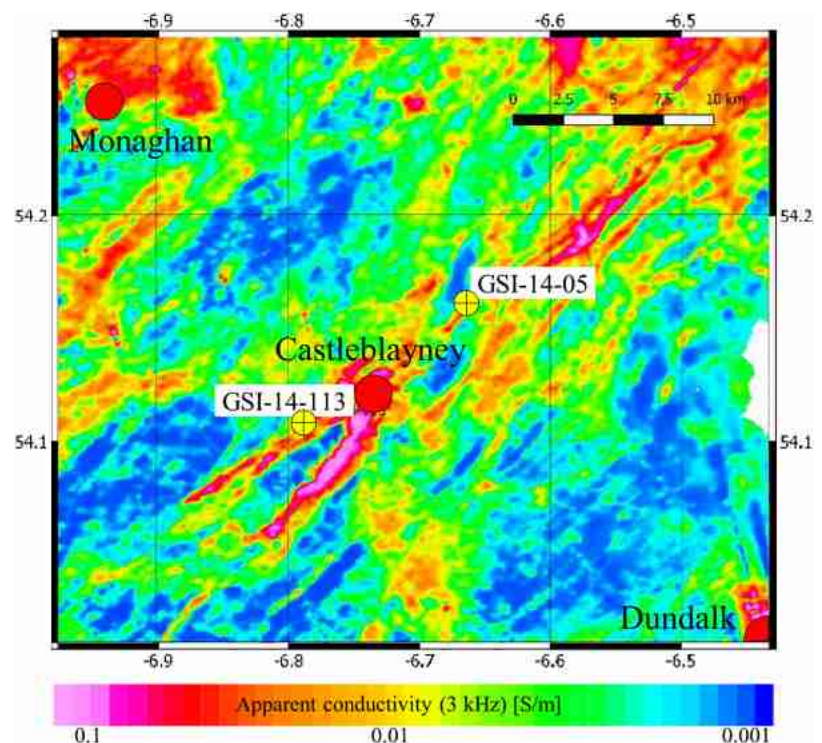
**Figure 1** Study area in the Republic of Ireland, geological map and location of the two boreholes GSI-14-113 and GSI-14-05.

domain measurements have been performed in the Republic of Ireland. The data were used to reassess the geology of the Moffat Shale Group, a complex geological structure located in the North of Ireland (Beamish *et al.* 2010; Fig. 1). In the cited publication, half-space estimates of subsurface conductivity were derived from the AEM data for mapping purposes. Near the Moffat Shales, these maps show high-conductivity

anomalies trending southwest to northeast, with an almost linear appearance (Fig. 2). Ground-based geophysical surveys supported the correlation between the occurrence of carbonaceous, pyritic rocks within the Moffat Shale Group and the conductivity anomalies (Cooper *et al.* 2016).

It is well known that carbonaceous rocks such as black shales and schists can bear strongly anomalous electrical

**Figure 2** Apparent conductivity data from 3 kHz airborne electromagnetic data acquired during the Tellus Programme (Beamish *et al.* 2010; Cooper *et al.* 2016).



properties regarding polarization and anisotropy (e.g. Jödicke *et al.* 2004; Bazin *et al.* 2018; Börner *et al.* 2018). So far, however, the electrical properties of the Moffat Shales are unknown. We consequently performed a laboratory study in order to provide additional laboratory-scale information for the interpretation of the AEM data. Rock material taken from two boreholes down to a depth of 71 m was investigated (Figs. 1 and 2). The complex-valued electrical conductivity of the rocks was determined by measurements of the spectral induced polarization (SIP) on oriented pairs of plugs. Geochemical analyses as well as the density and porosity determination provide additional information for the interpretation of the complex conductivity data, thereby focusing on polarization effects and anisotropy. The implications of the laboratory results for the interpretation of AEM data are assessed by performing one-dimensional forward simulations.

## GEOLOGICAL SETTING OF THE MOFFAT SHALE GROUP

The origin of the Moffat Shale Group has been under discussion for a long time. The most commonly accepted hypothesis explains its formation by an accretionary prism, which developed during the collision of the continents Avalonia and Laurentia due to the closure of the Iapetus Ocean in the late Silurian (approximately 418 Ma ago). In the course of the subduction process, marine sediments were scraped from the ocean floor and accreted to the Laurentian continent. This led to the formation of turbidite sequences, that is the segmentation into parallel tracts stretching from northeast to southwest, separated by strike-parallel faults (Mitchell 2004).

Each of those tracts includes an approximately 2 km thick sand- or mudstone succession, followed by a 150-m thick black shale sequence (Beamish *et al.* 2010). The black shales differ from the other mudstones by the presence of organic carbon, which originates from the organic matter of marine plants and animals (Uffmann, Littke and Rippen, 2012). The oxygen-poor environment required for the conservation of the carbonaceous material also provided good conditions for the formation of sulfide minerals, leading to an abundance of pyrite and chalcopyrite in the Moffat Shale (cf. Tucker 2001).

## ELECTRICAL PROPERTIES

The electrical conductivity  $\sigma^*$  of a rock is generally a frequency-dependent, complex-valued and anisotropic property (Olhoeft 1985; Nabighian 1987).

It can be understood as a superposition of an electrolytic  $\sigma_{el}$  and an interface  $\sigma_{if}^*$  conductivity.  $\sigma^*$  is related to the complex electrical resistivity  $\rho^*$  via the reciprocal:

$$\sigma^*(\omega) = \frac{1}{\rho^*(\omega)} = \sigma_{el} + \sigma_{if}^*(\omega), \quad (1)$$

where the  $*$  denotes complex quantities and  $\omega$  is the angular frequency. It may also be written in terms of real and imaginary part ( $\sigma'$  and  $\sigma''$ , respectively) or as magnitude ( $|\sigma^*|$ ) and phase shift ( $\varphi$ ):

$$\sigma^*(\omega) = \sigma'(\omega) + i\sigma''(\omega) = |\sigma^*| \cdot e^{i\varphi}. \quad (2)$$

Here  $i$  denotes the imaginary unit. The electrolytic conductivity is commonly described by Archie's law and includes conduction through the free water phase in a rock's pore space (Archie 1942; Schön 2015). In the fully water-saturated case, it depends on porosity  $\Phi$ , the empirical cementation exponent  $m$  and the pore water conductivity  $\sigma_w$ :

$$\sigma_{el} = \Phi^m \cdot \sigma_w. \quad (3)$$

The interface conductivity  $\sigma_{if}^*$  is caused by a variety of mineral-surface-related polarization phenomena (Marshall & Madden 1959). The basis of polarization phenomena is the property of many minerals to develop a surface charge. When in contact with electrolytic solutions, the so-called electrical double layer (EDL) forms in the electrolyte as a counterbalance of this surface charge (Helmholtz 1879; Revil & Glover 1997; Duval *et al.* 2002). When an external electric field is applied, conduction and polarization take place. Thereby, the polarization at metal or semiconductor – solution interfaces (where current flow through the interface takes place) and diffusion-related polarization phenomena at charged mineral surfaces (without current flow through the interface) can be differentiated (e.g. Marshall & Madden 1959). A direct identification of the dominant polarization mechanism in a rock is not possible only by electrical measurements.

Diffusion-related polarization includes several mechanisms, such as the polarization by the motion of charge carriers within the EDL (electrochemical polarization; e.g. Schwarz 1962; Leroy *et al.* 2008) and the polarization at narrow pore throats, where the neighbouring EDLs come close (membrane polarization; Marshall & Madden 1959; Bückner & Hördt 2013).

Polarization with current flow through the interface – the so-called electrode polarization – occurs, when electronically conductive or semiconductive minerals, such as graphite,

pyrite or chalcopryrite, are present in a rock (Pelton *et al.* 1978; Hupfer *et al.* 2015; Revil *et al.* 2015; Gurin *et al.* 2018). A strong charge separation at the mineral surfaces takes place due to the transfer from electrolytic (in the pore fluid) to electronic conduction or semiconduction (in the mineral grain). When electrode polarization is the dominant polarization mechanism,  $\sigma^*$  can often be described by the Cole–Cole model (Cole and Cole 1941; Pelton *et al.* 1978):

$$\sigma^*(\omega) = \sigma_0 \left[ 1 - m \left( 1 - \frac{1}{1 + (i\omega\tau)^c} \right) \right]^{-1}, \quad (4)$$

where  $\sigma_0$  is the DC conductivity (conductivity asymptote toward zero frequency),  $m$  [0..1] denotes the chargeability and is a measure for the polarization strength,  $\tau$  is the relaxation time and reflects the period of the strongest polarization, and  $c$  [0..1] is called frequency exponent and describes the broadness of the polarization peak.

In the case of more than one electrode-polarization source or if other polarization mechanisms (i.e. electrochemical and membrane polarization) are also dominant, it is no longer possible to describe the complex conductivity of a rock with equation (4) with adequate accuracy. The more flexible Debye decomposition approach is frequently used to obtain convenient and objective parameters for the interpretation of such data (Nordsiek and Weller 2008). A complex conductivity spectrum of arbitrary appearance is thereby represented by a summation of  $l$  Debye relaxations:

$$\sigma^*(\omega) = \sigma_0 \left[ 1 - \sum_l m_l \left( 1 - \frac{1}{1 + i\omega\tau_l} \right) \right]^{-1}, \quad (5)$$

with  $\sigma_0$  as DC conductivity,  $\tau_l$  as relaxation time of contribution  $l$  and  $m_l$  as chargeability of contribution  $l$ . Equation (4) can be considered as a special case of the Debye decomposition. In order to represent the data by few characteristic parameters, the total chargeability  $\sum m$  and the mean relaxation time  $\bar{\tau}$  are calculated from the decomposition as follows (Nordsiek and Weller 2008):

$$\sum m = \sum_l m_l, \quad (6)$$

$$\bar{\tau} = \exp \left( \frac{\sum_l m_l \ln(\tau_l)}{\sum_l m_l} \right). \quad (7)$$

In general, the Debye decomposition is an ill-posed inverse problem, introducing a dependency on the choice of the number of terms and the regularization, which renders it non-unique. Further transformations are often employed for inversion stability purposes, for example, the enforcement of non-negativity, other physical bounds, or computational

well behaviour (e.g. Weigand and Kemna 2016; Börner *et al.* 2017).

An anisotropic behaviour of conductivity is often observed, especially in foliated sedimentary or metamorphic rocks (e.g. Halisch *et al.* 2009; Revil *et al.* 2013; Kassab and Weller 2019). The origins of electrical anisotropy can be, for example, the deformation of pore space during compaction or the alignment of polarizable rock constituents with the foliation (e.g. Jödicke *et al.* 2004; Börner *et al.* 2018).

If anisotropy is present, the conductivity is described by a second-rank tensor  $\hat{\sigma}^*$  with – in the most general case – nine components:

$$\hat{\sigma}^* = \begin{bmatrix} \sigma_{xx}^* & \sigma_{xy}^* & \sigma_{xz}^* \\ \sigma_{yx}^* & \sigma_{yy}^* & \sigma_{yz}^* \\ \sigma_{zx}^* & \sigma_{zy}^* & \sigma_{zz}^* \end{bmatrix}. \quad (8)$$

The tensor is a positive-definite matrix, which is also symmetric in the case of dominant ohmic conduction processes (Dekker & Hastie 1980; Weidelt 1999; Marti 2014). The number of non-zero tensor components can therefore be reduced by means of the principle axis theorem to the three principle directions  $\bar{\sigma}_{xx}^*$ ,  $\bar{\sigma}_{yy}^*$  and  $\bar{\sigma}_{zz}^*$ :

$$\hat{\sigma}^* = \begin{bmatrix} \bar{\sigma}_{xx}^* & 0 & 0 \\ 0 & \bar{\sigma}_{yy}^* & 0 \\ 0 & 0 & \bar{\sigma}_{zz}^* \end{bmatrix}. \quad (9)$$

For pronouncedly and planar foliated rocks – such as many sedimentary rocks – transverse isotropic conditions apply, which further reduce the independent components of  $\hat{\sigma}^*$  to one in-plane ( $\sigma_{||}^*$ , parallel to the foliation) and one perpendicular ( $\sigma_{\perp}^*$ , perpendicular to the foliation) conductivity:

$$\hat{\sigma}^* = \begin{bmatrix} \sigma_{||}^* & 0 & 0 \\ 0 & \sigma_{||}^* & 0 \\ 0 & 0 & \sigma_{\perp}^* \end{bmatrix}. \quad (10)$$

Taking the direction of sedimentation and the dip angle into account, transverse isotropic media often occur in the form of vertical transverse isotropic or tilted transverse isotropic media. The strength of the anisotropy of any physical property  $P$  may then be quantified by a coefficient  $\lambda_P$  (Keller and Frischknecht 1966):

$$\lambda_P = \sqrt{\frac{P_{||}}{P_{\perp}}}, \quad (11)$$

where  $P_{||}$  and  $P_{\perp}$  are the property values parallel and perpendicular to the foliation, respectively.

## MATERIALS AND METHODS

### Rock samples

The focus of the laboratory study was to reveal the cause of the high apparent airborne electromagnetic (AEM) conductivities of the Moffat Shale Group. Therefore, rock material from two boreholes, which pass through the target formation (see GSI-14-05 and GSI-14-113 in Fig. 1) was investigated. The rocks can be assigned to three different geological formations, all of which belong to the Moffat Shale Group: the Lough Avaghon Formation (LA), the Oghill Formation (OL) and the Kehernaghkilly Formation (KY). The latter is predominantly composed of carbonaceous and pyritic black shale with significant carbon content and visible amounts of pyrite, whereas the plugs from the other two formations consist of ordinary mudstones with negligible carbon content and only sporadic pyrite inclusions (Table 1 and Fig. A1). All three formations show a clear stratification, which is tilted with respect to the borehole trajectory. Due to the deformation during genesis, the stratification dip angle varies locally in the formations.

The core samples originate from different depths, down to 71 m, comprising 23 cylindrical plugs of 2 cm diameter and 3 cm length (see Table 2 and Fig. A1). Wherever possible, oriented pairs of plugs – drilled vertically and horizontally relative to the core axis – were produced to allow for a local assessment of anisotropy. Four samples were crushed using a disk mill RS 200 to a particle size fraction  $\leq 63 \mu\text{m}$  in order to perform comparative spectral induced polarization (SIP) measurements and coulometric analyses. The matrix density and porosity of all samples were derived by the triple weighing method (e.g. Schön, 2015). An overview of the basic petrophysical and geochemical characteristics of all samples is given in Table 2.

### Spectral induced polarization measurements

The complex electrical conductivity of all samples was measured in the frequency range between  $10^{-4}$  and  $10^5$  Hz

using the SIP method. A SIP-QUAD instrument from Radic Research and a modular measuring cell were used. The measuring cell utilizes a four-electrode configuration (see Fig. B1). It is equipped with platinum net electrodes (C1 and C2) for current injection, which are placed in reservoir chambers filled with degassed sodium chloride solution ( $\sigma_w = 0.1 \text{ S/m}$  at  $20^\circ\text{C}$ ). The sample holder is placed between the reservoir chambers. The voltage is measured with platinum wire ring electrodes (P1 and P2), which are located in slots at the ends of the sample. For the unconsolidated samples, we used a vertical arrangement of the same sample holder with adapted chambers for C1 and C2. The potential measurement and the geometrical factor of both cell configurations are identical.

All samples, both plugs and crushed material, were saturated under vacuum for 48 hours with a degassed sodium chloride solution with an initial conductivity  $\sigma_w = 0.1 \text{ S/m}$  at  $20^\circ\text{C}$ . Short repressurization periods were applied to advance the wetting of the sample interior. After the saturation process, the samples were kept at normal conditions for minimum 24 hours to equilibrate. All plugs were wrapped in PTFE tape and placed tightly into the sample holder. Due to the very low measuring frequencies, a full SIP spectrum for a single sample took approximately 12 hours. The SIP response of each sample was monitored for at least 48 hours.

The resulting SIP spectra were processed by means of the Debye decomposition (cf. equation (5)). The implementation is the one described by Börner *et al.* (2017) expanded by the use of analytic derivatives for the computation of the Jacobian and a line search algorithm (see, e.g., Taran-tola 2005). The model space has been parameterized by five logarithmically equidistant relaxation times per decade ranging from  $10^{-7}$  to  $10^7$  seconds. Data affected by electromagnetic coupling effects were not used for the decomposition (above  $10^3$  Hz for the mudstones and above  $10^4$  Hz for the black shale). The characteristic parameters  $\sigma_0$ ,  $\sum m$  and  $\bar{\tau}$  were calculated for all samples (cf. equations (6) and (7), Table 2).

**Table 1** Overview of the formations covered by the presented dataset.  $\bar{d}_{ma}$  denotes average matrix density,  $\bar{\Phi}$  is average porosity and  $\bar{C}_{org}$  refers to the average amount of organic carbon

| Formation      | Rock type   | Borehole | $\bar{d}_{ma}$ (g/cm <sup>3</sup> ) | $\bar{\Phi}$ (%) | $\bar{C}_{org}$ (wt%) <sup>*</sup> | Pyrite   |
|----------------|-------------|----------|-------------------------------------|------------------|------------------------------------|--|
| Lough Avaghon  | Mudstone    | 14-113   | $2.70 \pm 0.01$                     | $1.15 \pm 0.15$  | $\approx 0.2$                      | Grains small and rare  |
| Oghill         | Mudstone    | 14-05    | $2.73 \pm 0.02$                     | $3.60 \pm 0.4$   | $\approx 0.05$                     | No pyrite visible  |
| Kehernaghkilly | Black shale | 14-05    | $2.74 \pm 0.1$                      | $1.25 \pm 0.63$  | $\approx 2$                        | Varying pyrite content ( $\approx 0$ – $10 \text{ vol}\%$ ) <sup>†</sup> |

<sup>\*</sup>From coulometry after Herrmann and Knake (1973).

<sup>†</sup>Rough overall estimate based on coulometric determination of the sulfur content and  $\bar{d}_{ma}$ .

**Table 2** Overview of the samples investigated in this study.  $d_{\text{ma}}$  denotes matrix density,  $\Phi$  is porosity

| Sample ID | Formation | Borehole | drill direction | Depth (m) | $\Phi$ (%) | $d_{\text{ma}}$ (g/cm <sup>3</sup> ) | Debye decomposition |            |                  |
|-----------|-----------|----------|-----------------|-----------|------------|--------------------------------------|---------------------|------------|------------------|
|           |           |          |                 |           |            |                                      | $\sigma_0$ (S/m)    | $\Sigma m$ | $\bar{\tau}$ (s) |
| LA-36-s   | LA        | 14-113   | Vertical        | 36.0      | 1.31       | 2.71                                 | 8.15E-04            | 2.45E-01   | 6.72E-03         |
| LA-39-h   | LA        | 14-113   | Horizontal      | 39.3      | 1.05       | 2.68                                 | 1.73E-03            | 1.41E-01   | 9.77E-03         |
| LA-39-v   | LA        | 14-113   | Vertical        | 39.3      | 0.98       | 2.69                                 | 4.90E-04            | 1.71E-01   | 3.79E-03         |
| OL-09-h   | OL        | 14-05    | Horizontal      | 9.1       | 3.74       | 2.71                                 | 8.83E-03            | 1.71E-01   | 1.24E-01         |
| OL-09-v   | OL        | 14-05    | Vertical        | 9.1       | 4.01       | 2.73                                 | 1.71E-03            | 1.19E-01   | 1.91E-02         |
| OL-18-h   | OL        | 14-05    | Horizontal      | 18.3      | 3.17       | 2.75                                 | 8.34E-03            | 1.69E-01   | 3.33E-01         |
| OL-18-v   | OL        | 14-05    | Vertical        | 18.3      | 4.02       | 2.71                                 | 1.94E-03            | 1.39E-01   | 6.12E-02         |
| KY-50-h   | KY        | 14-05    | Horizontal      | 49.5      | 1.94       | 2.73                                 | 5.83E-03            | 9.95E-01   | 8.52E+02         |
| KY-50-v   | KY        | 14-05    | Vertical        | 49.5      | 1.68       | 2.76                                 | 5.10E-03            | 9.95E-01   | 6.18E+02         |
| KY-55-h   | KY        | 14-05    | Horizontal      | 54.6      | 1.67       | 2.71                                 | 6.62E-03            | 9.93E-01   | 8.31E+02         |
| KY-55-v   | KY        | 14-05    | Vertical        | 54.6      | 1.72       | 2.81                                 | 2.74E-03            | 9.88E-01   | 2.83E+02         |
| KY-55-s   | KY        | 14-05    | Horizontal      | 54.6      | 1.27       | 2.68                                 | 3.35E-03            | 9.85E-01   | 9.79E+02         |
| KY-59-h   | KY        | 14-05    | Horizontal      | 58.5      | 1.68       | 2.68                                 | 4.67E-03            | 9.91E-01   | 4.54E+02         |
| KY-59-v   | KY        | 14-05    | Vertical        | 58.5      | 1.39       | 2.70                                 | 5.70E-03            | 9.88E-01   | 2.58E+02         |
| KY-59-s   | KY        | 14-05    | Horizontal      | 58.5      | 1.38       | 2.77                                 | 6.83E-03            | 9.92E-01   | 3.76E+02         |
| KY-61-h   | KY        | 14-05    | Horizontal      | 61.2      | 1.15       | 2.71                                 | 2.28E-03            | 9.40E-01   | 3.22E+02         |
| KY-61-v   | KY        | 14-05    | Vertical        | 61.2      | 1.35       | 2.76                                 | 2.30E-03            | 9.59E-01   | 5.72E+02         |
| KY-63-s   | KY        | 14-05    | Horizontal      | 63.0      | 1.31       | 2.77                                 | 3.61E-03            | 9.77E-01   | 5.37E+02         |
| KY-69-h   | KY        | 14-05    | Horizontal      | 69.0      | 1.86       | 2.75                                 | 4.19E-03            | 9.91E-01   | 5.86E+02         |
| KY-69-v   | KY        | 14-05    | Vertical        | 69.0      | 1.62       | 2.76                                 | 3.34E-03            | 9.92E-01   | 4.96E+02         |
| KY-69-s   | KY        | 14-05    | Vertical        | 69.0      | 1.01       | 2.84                                 | 8.67E-04            | 6.57E-01   | 5.61E+01         |
| KY-71-h   | KY        | 14-05    | Horizontal      | 70.8      | 0.77       | 2.64                                 | 1.49E-03            | 9.91E-01   | 5.35E+02         |
| KY-71-v   | KY        | 14-05    | Vertical        | 70.8      | 0.96       | 2.63                                 | 1.49E-03            | 9.67E-01   | 4.08E+02         |
| LA-39-v-c | LA        | 14-113   | Crushed         | 39.3      | ~40        | 2.69                                 | 1.30E-01            | 7.48E-03   | 6.91E-04         |
| OL-18-h-c | OL        | 14-05    | Crushed         | 18.3      | ~40        | 2.75                                 | 1.06E-01            | 5.87E-03   | 3.30E-03         |
| KY-71-h-c | KY        | 14-05    | Crushed         | 70.8      | ~40        | 2.64                                 | 1.12E-01            | 6.07E-02   | 1.48E-04         |
| KY-71-v-c | KY        | 14-05    | Crushed         | 70.8      | ~40        | 2.63                                 | 9.82E-02            | 6.99E-02   | 2.06E-04         |

### Synthetic airborne electromagnetic data

The laboratory measurements revealed a wide range of conductivities and polarization characteristics of the Moffat Shale Group. We consequently assessed whether the documented electrical properties can be the source of the anomalous AEM data (Fig. 2) by undertaking a one-dimensional (1D) forward modelling study. By carrying out simulations based on the complex conductivities from the laboratory experiments, a basic evaluation of the sensitivity of AEM to the observed material properties is possible. A Matlab implementation of the analytic solution to the Helmholtz equation for AEM was used to obtain theoretical AEM data produced by a given 1D complex conductivity distribution (pers. commu. Ralph-Uwe Börner; Nabighian 1987; Scheunert *et al.* 2016).

All calculations include the same parameterization of the measuring geometry, which is in accordance with the actual setup used during the AEM surveys of the Tellus

Programme. A horizontal magnetic dipole system (HMD) with vertical-coplanar coils was used with an offset between receiver and transmitter of 21.4 m. The flight altitude was set to 60 m, which was the usual height in rural areas.

A typical evaluation quantity in AEM with a HMD source is the angular component of the magnetic field (Nabighian 1987), which is normalized to the primary field (so it becomes dimensionless). The AEM convention is to split the dimensionless magnetic field into its real and imaginary component (typically denoted  $R$  and  $Q$ , respectively). If no conduction in the subsurface takes place, there is no secondary magnetic field, so the resulting magnetic field is equal to the primary field, which means  $R = 1$  and  $Q = 0$ . If conduction is present,  $R$  will be larger than 1 and  $Q$  larger than 0. In order to keep  $R$  and  $Q$  at similar values, 1 is subtracted from the component  $R$ , so when plotted, both  $R$  and  $Q$  are  $\geq 0$ .

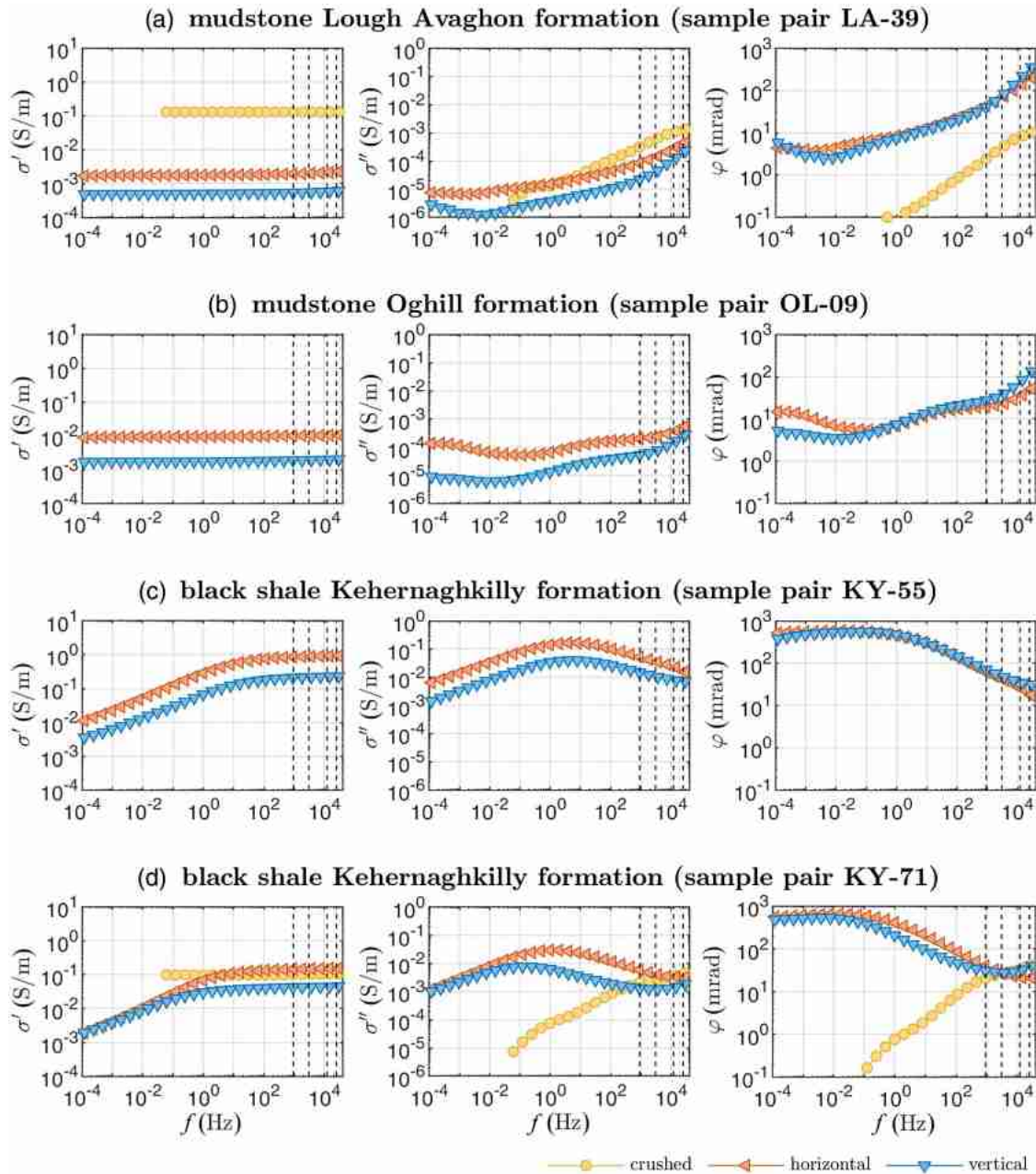


Figure 3 SIP spectra of oriented pairs of plugs and crushed material for the two mudstone formations (a and b) and the black shale at two different depths (c and d).

## RESULTS

### Frequency-dependent complex conductivity

Figure 3 shows both the real and imaginary part of the conductivity as well as the phase shift for two pairs of mudstone (OL-09 and LA-39, Figs 3a,b, respectively) and black shale (KY-71 and KY-55, Figs 3c,d, respectively) samples.

Where available, the data for the corresponding crushed sample are also shown.

The mudstones are characterized by an almost frequency-independent real conductivity and comparatively small imaginary parts ( $10^{-5}$  to  $10^{-4}$  S/m). Due to the absence of semi-conductive material or organic carbon (see Table 1), which could cause electrode polarization, this reversely indicates

polarization effects dominated by diffusion-related polarization (e.g. electrochemical and membrane polarization). Samples from both mudstone formations show similar electrical properties in both magnitude and frequency dynamics. Differences observed in the real part of conductivity probably originate from porosity (cf. equation (3) and Fig. 4c), which seems to be moderately depth dependent (Fig. 4a). The correlation between  $\sigma_0$  and  $\Phi$  is partly masked by anisotropy effects (see the following subsection). The Debye decomposition yields total chargeabilities between 0.1 and 0.25 and mean relaxation times between  $3 \times 10^{-3}$  and  $10^{-1}$  second, reflecting the moderate polarization strength and frequency dynamics.

The  $\sigma'$  of the crushed material is much higher than that of the plugs due to the increased porosity of the crushed and saturated rock material. However, the imaginary conductivity is comparable to the one of the plugs above  $10^{-1}$  Hz, which indicates that the polarization in the high-frequency range is not significantly linked to the texture (shape, alignment, distribution) of the mineral components, which is destroyed during crushing.

The black shale samples show very strong low-frequency polarization indicated by pronounced peaks in the imaginary part around 1 Hz and phase shifts with a magnitude of 500 mrad and more at frequencies below 0.1 Hz (Figs 3c,d). This corresponds to a strong increase of the real conductivity towards higher frequencies. The general polarization behaviour resembles the Cole–Cole type of polarization (cf. equation (4)) and is typical for graphite-bearing rocks (see Pelton *et al.* 1978; Börner *et al.* 2018). The pyrite can be ruled out as main source of the spectral induced polarization (SIP) response, since it develops polarization features with shorter relaxation times (<10 seconds; see, e.g., Pelton *et al.* 1978). It would further be expected to show a maximum phase shift around one order of magnitude lower than observed in this study (see, e.g., Hupfer *et al.* 2015). We therefore consider the pyrite polarization component to be masked by the graphite contribution. The black shale stands out from the mudstone formations with chargeabilities between  $0.66$  and  $0.995$  and mean relaxation times between  $5 \times 10^1$  and  $10^3$ .

When the black shale is crushed, that is the texture is destroyed and the largest coherent grain size is reduced to the particle size of the crushed material ( $\leq 63 \mu\text{m}$ ), the low-frequency polarization feature disappears completely (see imaginary conductivity and phase shift in Fig. 3d). This manifests itself in the form of a drop in imaginary conductivity by more than two orders of magnitude at 1 Hz, and – at high frequencies – an unchanged real-part conductivity. We can

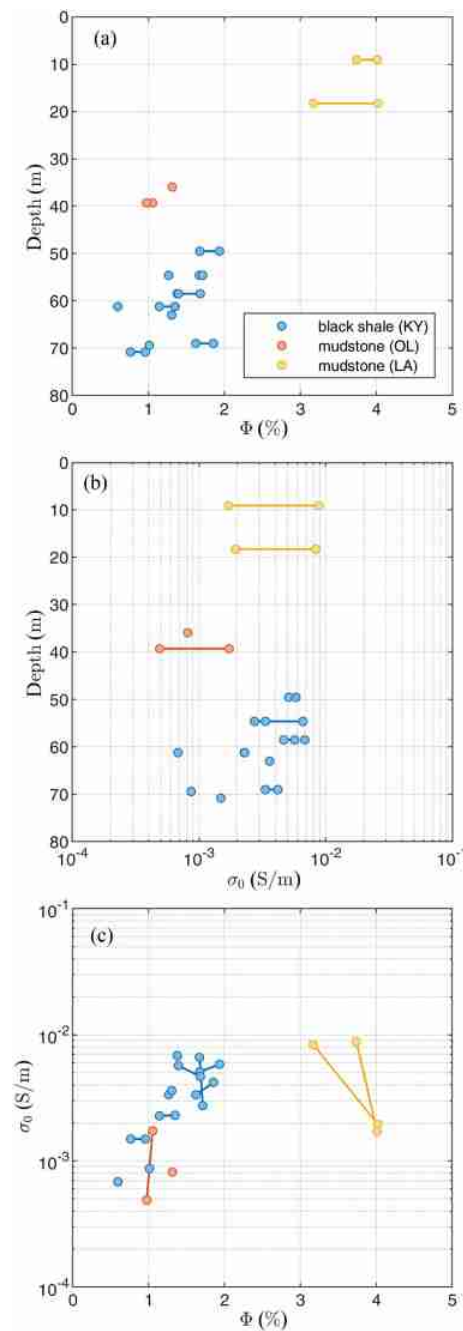


Figure 4 Porosity  $\Phi$  and DC conductivity  $\sigma_0$  versus depth and correlation between porosity and DC conductivity for all plugs (DC conductivity  $\sigma_0$  was obtained by Debye decomposition). Connecting lines mark sample pairs.

conclude from this behaviour that the graphite polarization is texture controlled and attributed to rock components with an effective length scale larger than the particle size of the crushed material.

**Table 3** Mean dip angle  $\theta$  and semiaxes (index “||” and “ $\perp$ ”, respectively) as well as anisotropy values  $\lambda$  of the Debye decomposition parameters calculated from the measurements on oriented sample pairs (see equations (5) and (11) as well as Figs 5 and C1)

| Sample pair<br>(v/h) | dip $\theta$ ( $^\circ$ ) | Anisotropic Debye decomposition parameter |                    |                      |                   |                      |                      |                        |                      |                        |
|----------------------|---------------------------|---|--------------------|----------------------|-------------------|----------------------|----------------------|------------------------|----------------------|------------------------|
|                      |                           | $\sigma_0$ (S/m)                          |                    |                      | $\Sigma m$        |                      |                      | $\bar{\tau}$ (seconds) |                      |                        |
|                      |                           | $\sigma_{0,  }$                           | $\sigma_{0,\perp}$ | $\lambda_{\sigma_0}$ | $(\Sigma m)_{  }$ | $(\Sigma m)_{\perp}$ | $\lambda_{\Sigma m}$ | $\bar{\tau}_{  }$      | $\bar{\tau}_{\perp}$ | $\lambda_{\bar{\tau}}$ |
| LA-39                | $11.8 \pm 3$              | 2.50E-03                                  | 5.00E-04           | 2.24                 | 1.40E-01          | 1.73E-01             | 0.90                 | 1.13E-02               | 3.70E-03             | 1.75                   |
| OL-09                | $7.5 \pm 1.5$             | 1.19E-02                                  | 1.70E-03           | 2.65                 | 1.72E-01          | 1.19E-01             | 1.20                 | 2.38E-01               | 1.90E-02             | 3.54                   |
| OL-18                | $9 \pm 1.5$               | 1.12E-02                                  | 1.90E-03           | 2.43                 | 1.70E-01          | 1.39E-01             | 1.11                 | 6.46E-01               | 6.05E-02             | 3.27                   |
| KY-50                | $21 \pm 1.5$              | 6.00E-03                                  | 5.00E-03           | 1.10                 | 9.95E-01          | 9.95E-01             | 1.00                 | 9.27E+02               | 5.94E+02             | 1.25                   |
| KY-55                | $14.6 \pm 2$              | 8.20E-03                                  | 2.70E-03           | 1.74                 | 9.93E-01          | 9.88E-01             | 1.00                 | 1.24E+03               | 2.75E+02             | 2.12                   |
| KY-59                | $63.5 \pm 2$              | 6.20E-03                                  | 4.40E-03           | 1.19                 | 9.87E-01          | 9.92E-01             | 1.00                 | 2.33E+02               | 8.21E+02             | 0.53                   |
| KY-61                | $20.5 \pm 3$              | 2.30E-03                                  | 2.30E-03           | 1.00                 | 9.37E-01          | 9.63E-01             | 0.99                 | 3.06E+02               | 7.09E+02             | 0.66                   |
| KY-69                | $29.7 \pm 2.5$            | 2.70E-03                                  | 1.80E-03           | 1.22                 | 9.95E-01          | 9.95E-01             | 1.00                 | 7.41E+03               | 5.62E+03             | 1.15                   |
| KY-71                | $12 \pm 5$                | 1.30E-03                                  | 1.20E-03           | 1.04                 | 9.92E-01          | 9.67E-01             | 1.01                 | 8.55E+02               | 7.74E+02             | 1.05                   |

### Anisotropy of spectral induced polarization parameters

An inspection of the raw data (Fig. 3) already shows a significant impact of the drilling direction on  $\sigma^*$ . Since they completely characterize the SIP response and intrinsically describe the frequency dependence of conductivity, we base our evaluation of anisotropy on the Debye decomposition parameters  $\sigma_0$ ,  $\Sigma m$  and  $\bar{\tau}$ . The fundamentals of anisotropy (equations (7)–(11)) hold also for  $\sigma_0$ ,  $\Sigma m$  and  $\bar{\tau}$ . Generally, the DC conductivity is larger and the mean relaxation time is longer for horizontally drilled samples. Total chargeability shows inconclusive tendencies. This is the case for all three formations (see Table 2).

To allow comparison with data from other rock formations, we must take into account that the drilling direction does not necessarily coincide with the foliation direction (see Fig. A1). Therefore, we measured the mean foliation dip angle with a protractor for the vertically drilled plugs. These dip angles were then assigned to the associated sample pairs (Table 3).

Based on a visual inspection of the plugs, we assume an electrical anisotropy in the sense of a tilted transverse isotropic (TTI) medium (see equations (7)–(11)). The horizontal plugs can be considered as being drilled approximately perpendicular to the axis of foliation rotation. Therefore, the principle directions of the physical properties (i.e. parallel and perpendicular to the foliation) as well as the anisotropy values  $\lambda$  may be computed based on the general equation for a centered ellipse, which is rotated about the origin of coordinates by the dip angle  $\theta$  (see also Fig. C1 for a graphical representation):

$$\left( \frac{y \cdot \sin \theta + x \cdot \cos \theta}{P_{||}} \right)^2 + \left( \frac{y \cdot \cos \theta - x \cdot \sin \theta}{P_{\perp}} \right)^2 = 1. \quad (12)$$

Here  $P_{||}$  and  $P_{\perp}$  denote the physical properties parallel and perpendicular to the foliation (see also equation (11)), respectively (i.e. the semiaxes of the ellipse). Every coordinate  $(x, y)$  fulfilling the equation is a member of the ellipse contour. Each sample pair represents two coordinates on the common anisotropy ellipse:  $(P_x, 0)$  and  $(0, P_y)$ , where  $P_x$  and  $P_y$  denote the physical properties of the plugs drilled horizontally and vertically, respectively (see Fig. C1). We therefore get two representations of equation (12) for one sample pair. Solving the resulting system of two equations yields  $P_{||}$  and  $P_{\perp}$ . Naturally, this data-processing approach only yields meaningful results, if the assumptions regarding directions and anisotropy type are sufficiently fulfilled.

The anisotropy ellipses for the DC conductivity  $\sigma_0$ , the mean relaxation time  $\bar{\tau}$  and the total chargeability  $\Sigma m$  are shown for all pairs versus depth in Fig. 5. A central line for each ellipse indicates the direction of foliation. For total chargeability, we plot the deviation of  $\Sigma m$  from 1 (i.e.  $(1 - \Sigma m)$ ). This emphasizes the  $\Sigma m$  differences between the black shale samples, which possess a  $\Sigma m$  larger than 0.93 (see Table 3). These small differences describe a significant variation in the SIP responses, as evidenced by the evaluation of the asymptotic behaviour of equation (4) for  $m \rightarrow 1$ .

All mudstone pairs show a strongly pronounced anisotropy of DC conductivity (indicated already in the raw data by the frequency-independent conductivity shift between vertical and horizontal samples; Figs 3a,b). A  $\lambda$  between 2.24 and 2.63 is found. The anisotropy of  $\bar{\tau}$  is even more pronounced with a maximum  $\lambda_{\bar{\tau}}$  of 3.54. The anisotropic behaviour of the black shale formation is similar.  $\sigma_0$  and  $\bar{\tau}$  show larger values parallel to the foliation than perpendicular

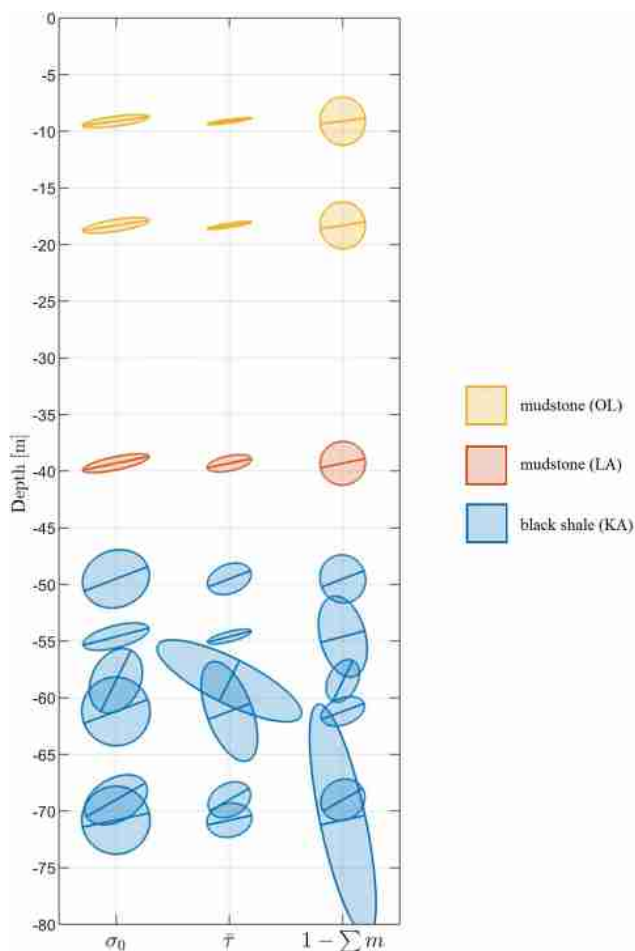


**Figure 5** Normalized anisotropy ellipses of Debye decomposition parameters  $\sigma_0$ ,  $\tau$ , and  $\Sigma m$  computed after equation (12) versus sampling depth (Table 3). Note that for total chargeability the anisotropy of  $(1 - \Sigma m)$  is plotted to visualize the small variations in  $\Sigma m$  close to 1, which have significant influence on  $\sigma^*$  (see equation (4)). A line for each ellipse indicates the direction of foliation. Colors denote formation: yellow, mudstone (OL, samples from GSI 14-05); orange, mudstone (LA, samples from GSI 14-113); blue, black shale (KA, samples from GSI 14-05).

thereto, although the degree of anisotropy is less (i.e. smaller  $\lambda$  values). Similarly, total chargeability is larger parallel to the foliation for most black shale pairs. Variations and deviations from the general formation behaviour can be caused by large, single pyrite inclusions or a highly local folding within the plug. In this case, the assumptions of a TTI medium are significantly violated and the applied approach is not valid anymore.

## DISCUSSION

### Anisotropy mechanisms and complex conductivity classification

The anisotropy found in the presented dataset can be related to two mechanisms. Firstly, the mudstone formations possess enlarged  $\sigma_0$  and  $\bar{\tau}$  parallel to the foliation, which is in accordance with earlier considerations regarding the effect of tortuosity on electrical conductivity (e.g. Kozeny 1927; Pape, Riepe and Schopper 1982; Revil *et al.* 2013; Müller-Huber, Schön and Börner 2015). Pore space and consequently current flow channels deform during compaction, which leads to a decreased tortuosity parallel to the foliation that enhances an efficient current flow (e.g. Revil *et al.* 2013). The same effect results in larger diffusion lengths longitudinal to the rock lamination and consequently longer mean relaxation times.

On the other hand, the black shale shows an anisotropy with enlarged  $\sigma_0$  and  $\bar{\tau}$  parallel to the foliation too, but it is less pronounced. At the same time, polarization is much stronger than in the mudstones. We relate this to the graphite in the samples, which is known to form plate-like textures aligning during formation and compaction (e.g. Börner *et al.* 2018). In this case, the elongated polarizable component causes an increased  $\bar{\tau}$  parallel to the foliation. The diffusion length scale of the graphite particles is not necessarily the same as that of the tortuous pore space. Furthermore, most samples contain varying amounts of nearly spherical pyrite inclusions. Both effects together can explain the reduced anisotropy strength in the black shale formation.

Our findings regarding  $\sigma_0$  and  $\bar{\tau}$  of the black shale are in good agreement with other studies (Fig. 6). Börner *et al.* (2018) investigated the complex electrical conductivity of a metamorphic black schist and found the polarization component dedicated to graphite to be characterized by very high chargeabilities ( $m = 0.997$ ) and long relaxation times ( $\tau = 3 \times 10^4$  second). Also the reduced relaxation time perpendicular to the foliation has been found in that study. The similarities regarding the electrical appearance of graphite are remarkable since the two rocks are very different with respect to their geological history. The  $\bar{\tau}$  from this study tends to be smaller by approximately one order of magnitude, which is a manifestation of the pyrite content (cf. smaller relaxation times of sulfide deposits in Fig. 6; see also Hupfer *et al.* 2015). A strong variation in chargeability of the crushed sample between black shale and schist is likely related to the varying graphite content (cf. Table 1). Earlier results from Pelton *et al.* (1978) also found graphite deposits to be associated with high

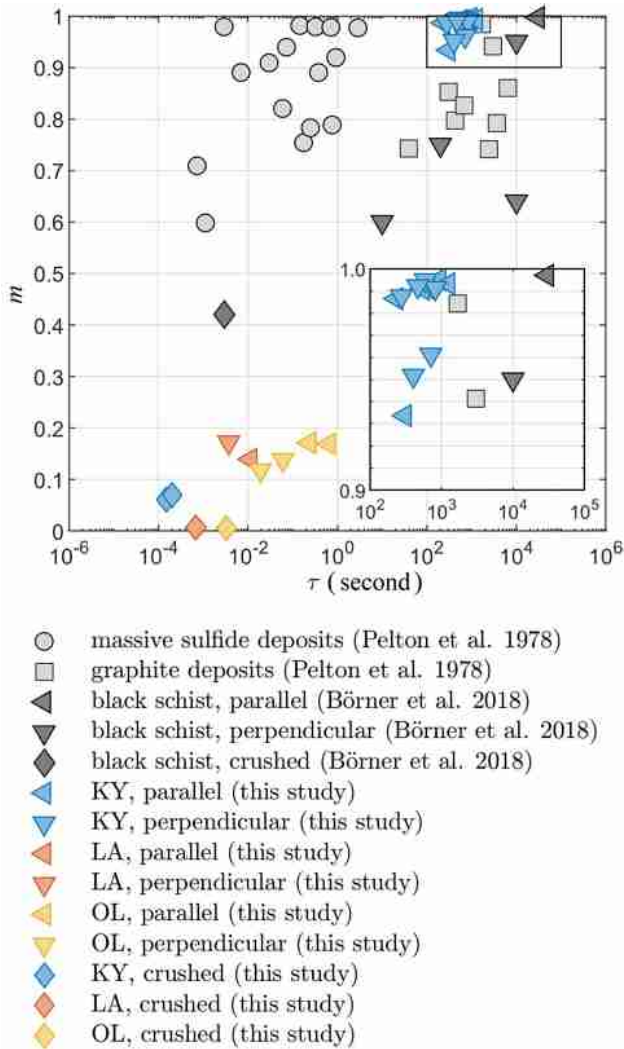


Figure 6 Black shale anisotropy compared to other studies in the  $\tau$ - $m$  plane (data from Table 3; crushed material data from Table 2).

chargeabilities and relaxation times, which are clearly distinguishable from, for example pyritic (sulfide) deposits. The investigated mudstones can clearly be classified as carbon free in the  $\tau$ - $m$  plane due to their low chargeability and mean relaxation time, which was confirmed by the geochemical analyses (cf. Table 1).

#### Implications for airborne electromagnetic

For the 1D forward modelling study the airborne electromagnetic (AEM) response (represented as  $R$  and  $Q$ ) was calculated for several conductivity scenarios and for a wide range of frequencies ( $10^0$  Hz to  $10^8$  Hz). The AEM data consequently

appear as spectra, which bear some similarity to the spectral induced polarization (SIP) spectra (Fig. 7). However, the complex and frequency-dependent nature of the AEM response is the result of electromagnetic induction and conduction in general and not necessarily a manifestation of polarization in the SIP sense.

At first, the manifestation of a frequency-dependent complex half-space conductivity on the AEM response is demonstrated (Fig. 7a). Two half-spaces with conductivities following a Cole-Cole polarization (equation (4)) with varying relaxation times were calculated (blue and red lines). All other Cole-Cole parameters are constant ( $\sigma_0 = 0.002$  S/m,  $m = 0.99$ ,  $c = 0.45$ ). For comparison, two half-space models with real-valued, scalar conductivity that use the absolute value of the complex-valued Cole-Cole conductivity, evaluated at a typical AEM measuring frequency of 12 kHz, are shown (red and blue circles). The computations show that for the long  $\tau$  the Cole-Cole half-space (red, solid line) produces almost the same response as the associated real-valued half-space (red circles). The polarization effects occur in a low-frequency range, where no induction takes place given the AEM setup. Therefore, no interference of the two effects takes place. It cannot be derived from the AEM data, whether they are exclusively influenced by electrolytic (and therefore real-valued) conduction, or if polarization effects play a major role. This might lead to ambiguities in the geological implications of those data. Performing the AEM measurements at various frequencies does not solve this problem at all, since the effect is similar for all AEM typical frequencies.

The model with  $\tau = 0.1$  s (blue line) shows a completely different behaviour. The induction in the subsurface takes place at the same frequencies at which polarization occurs, so that both effects interfere with each other. The Cole-Cole model (blue line) produces a steep slope in  $R$  and a high peak in  $Q$  that cannot be explained by the corresponding real-valued half-space (blue circles). The two extreme cases shown in Fig. 7(a) demonstrate that it depends on the relaxation time of the material whether AEM can differentiate between polarization and simple conduction.

In a second step, we now look at the situation of the investigated Moffat Shale. Figure 7(b) shows the AEM response of a two-layer half-space (green, solid line), which represents the situation at the investigated borehole GSI-14-05 in a simplified manner. A 30-m thick mudstone layer (approximated by  $|\sigma^*| = 0.002$  S/m and  $\varphi = 30$  mrad, both frequency independent) covers a half-space consisting of black shale (Cole-Cole parameterization with  $\sigma_0 = 0.002$  S/m,  $m = 0.99$ ,  $\tau = 10^3$  seconds,  $c = 0.45$ ). The layered model (green line) can

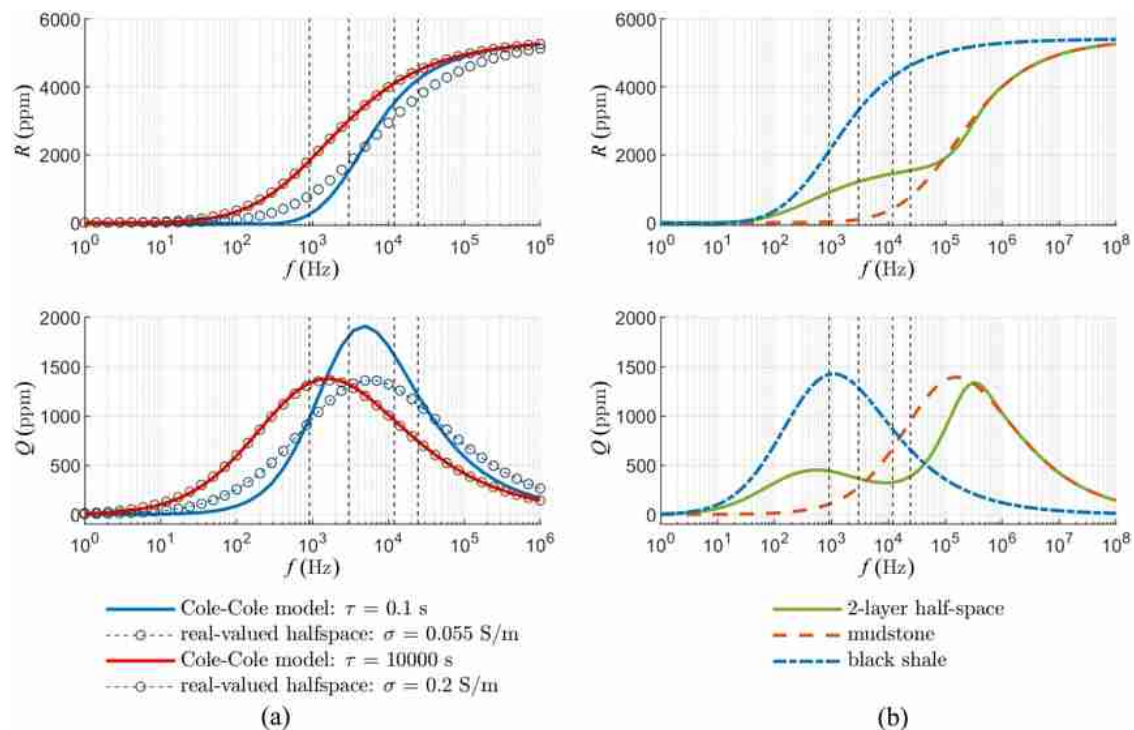


**Figure 7** (a) Synthetic AEM data for complex-valued and real-valued homogeneous half-spaces; (b) synthetic AEM data for two homogeneous half-spaces and the two-layer case representing the situation in the study area. The AEM measuring frequencies are indicated by the black dashed lines (see the text for details).

clearly be interpreted as a combination of the two half-spaces (blue and orange dashed lines). This is possible, since in this case the requirements of an increase in conductivity with increasing depth as well as a conveniently located layer boundary (within the depth of investigation of AEM) are fulfilled. The three models are therefore clearly distinguishable by their AEM response for the frequencies used during the Tellus AEM surveys (vertical dashed lines). Strong responses in  $R$  are very likely to be related to a subsurface consisting of black shale, whereas weak responses should be dedicated to mudstones. Intermediate values between those two extremes could be interpreted as a black shale half-space that is overlain by a thin (in the order of a few tens of meters) mudstone layer. However, no information about the polarization behaviour can be derived from AEM measurements without the *a priori* information from laboratory experiments.

## CONCLUSIONS

We carried out a laboratory study aiming to petrophysically characterize the Moffat Shale Group using material from two boreholes. The investigations included density and porosity as well as spectral induced polarization (SIP) measurements

on 23 oriented samples in the frequency range from  $10^{-4}$  to  $10^5$  Hz.

The sample material can be categorized into two groups. The carbon-free mudstone formations show weakly frequency-dependent, porosity-driven electrical conductivities with strong anisotropy. It can be explained by the deformation of pore channels by compaction and is in accordance with findings from other studies. On the other hand, the carbonaceous and pyritic black shale is characterized by moderately anisotropic but strong polarization effects producing high phase shifts especially at low frequencies, and a strong conductivity increase towards higher frequencies. Complementary SIP measurements and geochemical analyses on the crushed material lead to the conclusion that polarization is controlled by the texture and volume fraction of polarizable components.

The SIP data have been processed using a Debye decomposition approach. The complex electrical anisotropy was determined by utilizing the foliation dip angle and assuming tilted transverse isotropic conditions. The anisotropic characteristic decomposition parameters could then be used to show that our findings correspond well to other carbonaceous formations. Laboratory investigations on plugs from multiple

directions would allow for the reconstruction of the conductivity tensor without assuming an anisotropy regime and could help to better understand the interplay of the anisotropic Debye decomposition parameters and therefore enhance our understanding of the anisotropic complex conductivity.

One-dimensional simulations of airborne electromagnetic (AEM) data demonstrated that strongly polarizable rocks may only be distinguished in AEM when the polarization takes place in the sensitive frequency range ( $Q > 0$ ). Rocks with low-frequency polarization such as the black shale appear as highly conductive in AEM. Revealing that the cause of high conductivity is polarization requires additional information such as laboratory measurements or other *a priori* information.


## ACKNOWLEDGEMENTS

The authors thank the Geological Survey Ireland for the provision of the sample material and the constant support. Lukas Römhild thanks for funding by the European Union (EU) - European Social Fund (ESF), GEOSax project, application number 100310486. Jana H. Börner and Martin Sonntag thank for funding by the German Research Foundation (DFG, grant numbers SP 356/14-1 and SP 356/14-2 respectively). Duygu Kiyani thanks for funding through a research grant from the Science Foundation Ireland under grant number 13/RC/2092. The authors further thank Ralph-Uwe Börner for providing an implementation of the airborne electromagnetic analytic solution and his assistance in improving the Debye-decomposition code. We thank Matthias Halisch and one anonymous reviewer for helping to improve this manuscript.

## ORCID

D. Kiyani  <https://orcid.org/0000-0001-6024-5366>

V. Rath  <https://orcid.org/0000-0001-9558-6726>

J.H. Börner  <https://orcid.org/0000-0002-0117-7225>

## REFERENCES

- Anschütz H., Bazin S., Kasin K., Pfaffhuber A. and Smaavik T. 2017. Airborne mapping of sensitive clay-stretching the limits of AEM resolution and accuracy. *Near Surface Geophysics* **15**, 467–474.
- Arab-Amiri A.R., Moradzadeh A., Fathianpour N. and Siemon B. 2010. Inverse modeling of HEM data using a new inversion algorithm. *International Journal of Mining Reclamation and Environment* **1**, 9–20.
- Archie G.E. 1942. The electrical resistivity log as an aid in determining some reservoir characteristics. *Transactions of the American Institute of Mining, Metallurgical and Petroleum Engineers* **146**, 54–62.
- Auken E., Christiansen A.V., Kirkegaard C., Fiandaca G., Schamper C., Behroozmand A.A., *et al.* 2015. An overview of a highly versatile forward and stable inverse algorithm for airborne, ground-based and borehole electromagnetic and electric data. *Exploration Geophysics* **46**, 223–235.
- Avdeev D.B., Kuvshinov A.V., Pankratov O.V. and Newman G.A. 1998. Three-dimensional frequency-domain modeling of airborne electromagnetic response. *Exploration Geophysics* **29**, 111–119.
- Bazin S., Lysdahl A., Viezzoli A., Günther T., Anschütz H., Scheibz J., *et al.* 2018. Resistivity and chargeability survey for tunnel investigation: a case study on toxic black shale in Norway. *Near Surface Geophysics* **16**, 1–11.
- Beamish D., Kimbell G., Stone P. and Anderson T. 2010. Regional conductivity data used to reassess Lower Palaeozoic structure in the Northern Ireland sector of the Southern Uplands-Down-Longford terrane. *Journal of the Geological Society* **167**, 649–657.
- Börner J.H., Herdegen V., Repke J.-U. and Spitzer K. 2017. Spectral induced polarization of the three-phase system CO<sub>2</sub>-brine-sand under reservoir conditions. *Geophysical Journal International* **208**, 289–305.
- Börner J., Girault F., Bhattarai M., Adhikari L., Deldicque D., Perrier F., *et al.* 2018. Anomalous complex electrical conductivity of a graphitic black schist from the Himalayas of Central Nepal. *Geophysical Research Letters* **45**, 3984–3993.
- Bücker M. and Hördt A. 2013. Analytical modelling of membrane polarization with explicit parametrization of pore radii and the electrical double layer. *Geophysical Journal International* **194**, 804–813.
- Cole K.S. and Cole, R.H. 1941. Dispersion and absorption in dielectrics - I. Alternating current characteristics. *The Journal of Chemical Physics* **9**, 341–351.
- Cooper M., Floyd J., Barker G., Ture M., Hodgson J., McConnell B., *et al.* 2016. The geological significance of electrical conductivity anomalies of the Ordovician-Silurian Moffat Shale Group, Northern Ireland. In: *Unearthed: Impacts of the Tellus Surveys of the North of Ireland* (ed M.E. Young), pp. 169–178. Royal Irish Academy, Dublin, Ireland.
- Dekker D.L. and Hastie L.M. 1980. Magneto-telluric impedances of an anisotropic layered Earth model. *Geophysical Journal International* **61**, 11–20.
- Duval Y., Mielczarski J.A., Pokrovsky O.S., Mielczarski E. and Ehrhardt J.J. 2002. Evidence of the existence of three types of species at the quartz-aqueous solution interface at pH 0–10: XPS surface group quantification and surface complexation modeling. *Journal of Physical Chemistry B* **106**, 2937–2945.
- Fountain D. 1998. Airborne electromagnetic systems—50 years of development. *Exploration Geophysics* **29**, 1–11.
- Götze H.J., Afanasjew M., Alvers M., Barrio-Alvers L., Börner R.-U., Brandes C., *et al.* 2014. Towards an integrative inversion and interpretation of airborne and terrestrial data. In: *Tomography of the Earth's Crust: From Geophysical Sounding to Real-Time Monitoring* (eds M. Weber and U. Münch), pp. 21–41. Advanced Technologies in Earth Sciences. Springer.

- Gurin G., Ilyin Y., Nilov S., Ivanov D., Kozlov E., and Titov K. 2018. Induced polarization of rocks containing pyrite: Interpretation based on X-ray computed tomography. *Journal of Applied Geophysics* **154**, 315–325.
- Halisch M., Weller A., Sattler C.-D., Debschütz W. and El-Sayed A. M. 2009. A complex core-log case study of an anisotropic sandstone, originating from Bahariya Formation, Abu Gharadig Basin, Egypt, *Petrophysics* **50**, 478–497.
- Helmholtz H., 1879. Studien über electrische Grenzsichten. *Annalen der Physik* **243**, 337–382.
- Hupfer S., Martin T., Weller A., Günther T., Kuhn K., Djotsa Nguimeya Ngninjo V., et al. 2015. Polarization effects of unconsolidated sulphide-sand-mixtures. *Journal of Applied Geophysics* **135**, 456–465.
- Herrmann A.G. and Knake, D. 1973. Coulometrisches Verfahren zur Bestimmung von Gesamt-, Carbonat- und Nicht-carbonat-Kohlenstoff in magmatischen, metamorphen und sedimentären Gesteinen. *Zeitschrift Analytische Chemie* **266**, 196–201.
- Jödicke H., Kruhl J.H., Ballhaus C., Giese P. and Untiedt, J. 2004. Syngenetic, thin graphite-rich horizons in lower crustal rocks from the Serre San Bruno, Calabria (Italy), and implications for the nature of high-conducting deep crustal layers. *Physics of the Earth and Planetary Interiors* **141**, 37–58.
- Kassab M.A. and Weller A. 2019. Anisotropy of permeability, P-wave velocity and electrical resistivity of Upper Cretaceous carbonate samples from Tushka Area, Western Desert, Egypt. *Egyptian Journal of Petroleum*, **28**, 189–196.
- Keller G., Frischknecht F. 1966. *Electrical Methods in Geophysical Prospecting*. Pergamon Press.
- Kiyan D., Rath V. and Delhay R. 2017. An inversion toolbox for frequency- and time-domain airborne electromagnetic data from surveys in Ireland. EAGE, the Second European Airborne Electromagnetics Conference in Malmö, Sweden, 7 September, 2017, Extended Abstract.
- Kozeny J. 1927. *Über kapillare Leitung des Wassers im Boden*. Akademie der Wissenschaft Wien **136**, 271–306.
- Kratzer T. and Macnae J.C. 2012. Induced polarization in airborne EM. *Geophysics* **77**, E317–E327.
- Leroy P., Revil A., Kemna A., Cosenza, A. and Ghorbani A. 2008. Complex conductivity of water-saturated packs of glass beads. *Journal of Colloid and Interface Science* **321**, 103–117.
- Li D., Wang Y., Lin J., Yu S. and Ji Y. 2017. Electromagnetic noise reduction in grounded electrical-source airborne transient electromagnetic signal using a stationary wavelet-based denoising algorithm. *Near Surface Geophysics* **15**, 163–173.
- Lin C., Fiandaca G., Auken E., Couto M.A. and Christiansen A.V. 2019. A discussion of 2D induced polarization effects in airborne electromagnetic and inversion with a robust 1D laterally constrained inversion scheme. *Geophysics* **84**, E75–E88.
- Liu Y., Yin C. 2014. 3D anisotropic modeling for airborne EM systems using finite-difference method. *Journal of Applied Geophysics* **109**, 186–194.
- Marshall D.J. and Madden T.R. 1959. Induced polarization, a study of its causes. *Geophysics* **4**, 790–816.
- Martí A. 2014. The role of electrical anisotropy in magnetotelluric responses: from modelling and dimensionality analysis to inversion and interpretation. *Surveys in Geophysics* **35**, 179–218.
- McMillan S.M., Haber, E. and Marchant D. 2018. Large scale 3D airborne electromagnetic inversion – recent technical improvements. 26th AEGC Conference, Sydney, Australia, 18 February, 2018, Extended Abstract.
- Mitchell W. 2004. *The Geology of Ireland – Our Natural Foundation*, 2 ed. Geological Survey of Northern Ireland, Belfast.
- Müller-Huber E., Schön J.H. and Börner F. 2015. The effect of a variable pore radius on formation resistivity factor. *Journal of Applied Geophysics* **116**, 173–176.
- Nabighian M. N. (ed.). 1987. *Electromagnetic Methods in Applied Geophysics - Theory. Volume 1*. Society of Exploration Geophysicists, Tulsa.
- Nordsiek S. and Weller A. 2008. A new approach to fitting induced-polarization spectra. *Geophysics* **73**, F235–F245.
- Olhoeft G.R. 1985. Low-frequency electrical properties. *Geophysics* **50**, 2492–2503.
- Pape H., Riepe M. and Schopper J.R. 1982. A pigeon-hole model for relating permeability to specific surface. *The Log Analyst* **23**, 5–13.
- Pelton W., Ward S., Hallof P., Sill W. and Nelson P. 1978. Mineral discrimination and removal of inductive coupling with multifrequency IP. *Geophysics* **43**, 588–609.
- Pfaffhuber A., Hendricks S. and Kvistedal Y. 2012. Progressing from 1D to 2D and 3D near-surface airborne electromagnetic mapping with a multisensor, airborne sea-ice explorer. *Geophysics* **77**, 109–117.
- Revil A. and Glover P.W.J. 1997. Theory of ionic-surface electrical conduction in porous media. *Physical Review B* **55**, 1757–1773.
- Revil A., Woodruff W.F., Torres-Verdín C. and Prasad M. 2013. Complex conductivity tensor of anisotropic hydrocarbon bearing shales and mudrocks. *Geophysics* **76**, D403–D418.
- Revil A., Florsch N. and Mao D. 2015. Induced polarization response of porous media with metallic particles—Part 1: A theory for disseminated semiconductors. *Geophysics* **80**, D252–D538.
- Schön J. 2015. *Physical Properties of Rocks—Fundamentals and Principles of Petrophysics*, 2nd ed. Handbook of Geophysical Exploration, Vol. 18. Elsevier.
- Scheunert M., Ullmann A., Afanasjew M., Börner R.-U., Siemon B. and Spitzer K. 2016. A cut-&-paste strategy for the 3-D inversion of helicopter-borne electromagnetic data - I. 3D inversion using the explicit Jacobian and a tensor-based formulation. *Journal of Applied Geophysics* **129**, 209–211.
- Schwarz G., 1962. A theory of the low-frequency dielectric dispersion of colloidal particles in electrolyte solution. *Journal of Physical Chemistry* **66**, 2636–2642.
- Siemon B., Christiansen A.V., Auken E. 2009a. A review of helicopter-borne electromagnetic methods for groundwater exploration. *Near Surface Geophysics* **7**, 629–646.
- Siemon B., Auken E., Christiansen A.V. 2009b. Laterally constrained inversion of helicopter-borne frequency-domain electromagnetic data. *Journal of Applied Geophysics* **67**, 259–268.
- Tarantola A. 2005. *Inverse Problem Theory and Methods for Model Parameter Estimation*. Other Titles in Applied Mathematics, Vol. 89. SIAM, Philadelphia.

Tucker M. 2001. *Sedimentary Petrology - An Introduction to the Origin of Sedimentary Rocks*, 3rd ed. Blackwell Science, Oxford.

Uffmann A., Littke R. and Rippen, D. 2012. Mineralogy and geochemistry of Mississippian and Lower Pennsylvanian black shales at the northern margin of the Variscan mountain belt (Germany and Belgium). *International Journal of Coal Geology* 103, 92–108.

Weidelt P. 1999. 3D conductivity models: implications of electrical anisotropy. In: *Three-Dimensional Electromagnetics* (eds M. Oristaglio and B. Spies), pp 119–137. SEG.

Weigand M. and Kemna A. 2016. Relationship between Cole–Cole model parameters and spectral decomposition parameters derived from SIP data, *Geophysical Journal International* 205, 1414–1419.

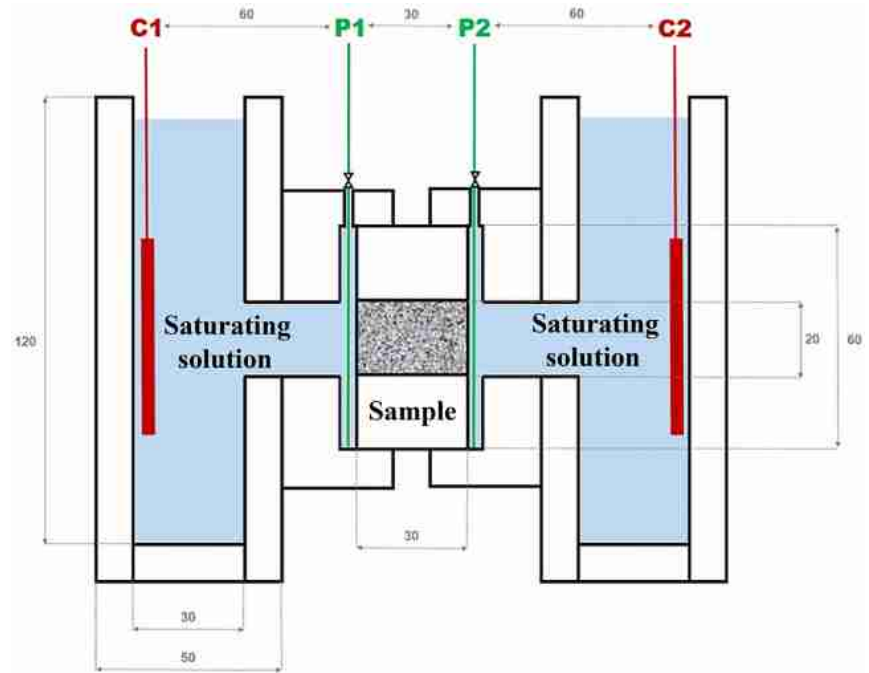
## APPENDIX A: FORMATIONS



Figure A1 Photographs of selected plugs from all three formations.

## APPENDIX B: SCHEME OF MEASURING CELL

**Figure B1** Scheme of modular measuring cell (cross section). The current flow is maintained by the net electrodes C1 and C2 (red), the voltage is measured at P1 and P2 (green), which are placed in slots at the ends of the sample. The interior is filled with NaCl solution (blue). All sizes are given in millimetres.



## APPENDIX C: ANISOTROPY ELLIPSE DETERMINATION

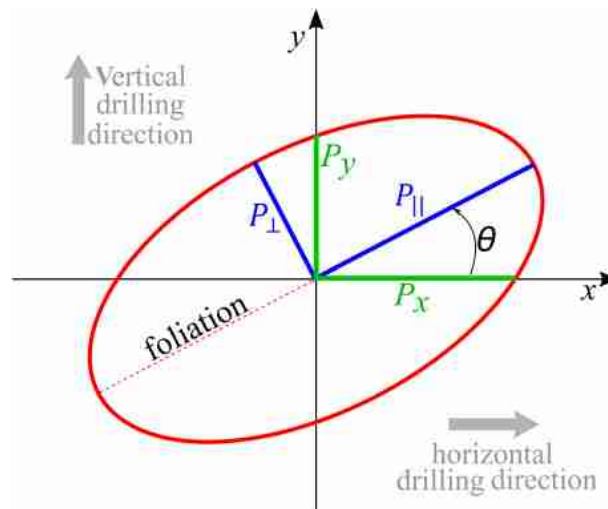


**Figure C1** Notation for the anisotropy ellipses.  $P_{\parallel}$  and  $P_{\perp}$  denote the physical properties parallel and perpendicular to the foliation, respectively.  $P_x$  and  $P_y$  denote the measured physical properties of the plugs drilled horizontally and vertically, respectively. The angle  $\theta$  is the dip.